

Phonon resonance modulation in weak van der Waals heterostructures: Controlling thermal transport in graphene-silicon nanoparticle systems

Yi Li(李毅), Yinong Liu(刘一浓), and Shiqian Hu(胡世谦)

Citation: Chin. Phys. B, 2024, 33 (**4**): 047401. DOI: 10.1088/1674-1056/ad1501
Journal homepage: http://cpb.iphy.ac.cn; http://iopscience.iop.org/cpb

What follows is a list of articles you may be interested in

Ultralow-temperature heat transport study of noncentrosymmetric superconductor CaPtAs

Yimin Wan(万一民), Erjian Cheng(程二建), Yuxin Chen(陈宇鑫), Chengcheng Zhao(赵成成), Chengpeng Tu(涂成鹏), Dongzhe Dai(戴东喆), Xiaofan Yang(杨小帆), Lu Xin(辛路), Wu Xie(谢武), Huiqiu Yuan(袁辉球), and Shiyan Li(李世燕)

Chin. Phys. B, 2023, 32 (**12**): 127403. DOI: 10.1088/1674-1056/ad02e9

Advances in thermoelectric $(GeTe)_x(AgSbTe_2)_{100-x}$

Hongxia Liu(刘虹霞), Xinyue Zhang(张馨月), Wen Li(李文), and Yanzhong Pei(裴艳中)

Chin. Phys. B, 2022, 31 (**4**): 047401. DOI: 10.1088/1674-1056/ac3cae

Two-dimensional square-Au_2S monolayer: A promising thermoelectric material with ultralow lattice thermal conductivity and high power factor

Wei Zhang(张伟), Xiao-Qiang Zhang(张晓强), Lei Liu(刘蕾), Zhao-Qi Wang(王朝棋), and Zhi-Guo Li(李治国)

Chin. Phys. B, 2021, 30 (**7**): 077405. DOI: 10.1088/1674-1056/abe115

Fabrication and characterization of Al-Mn superconducting films for applications in TES bolometers

Qing Yu(余晴), Yi-Fei Zhang(张翼飞), Chang-Hao Zhao(赵昌昊), Kai-Yong He(何楷泳), Ru-Tian Huang(黄汝田), Yong-Cheng He(何永成), Xin-Yu Wu(吴歆宇), Jian-She Liu(刘建设), and Wei Chen(陈炜)

Chin. Phys. B, 2021, 30 (**7**): 077402. DOI: 10.1088/1674-1056/abe0c6

Thermal stability and thermoelectric properties of Cd-doped nano-layered Cu_2Se prepared using NaCl flux method

Jianhua Lu(陆建华), Decong Li(李德聪), Wenting Liu(刘文婷), Lanxian Shen(申兰先), Jiali Chen(陈家莉), Wen Ge(葛文), and Shukang Deng(邓书康)

Chin. Phys. B, 2020, 29 (**12**): 127403. DOI: 10.1088/1674-1056/abbbf5

SPECIAL TOPIC — Heat conduction and its related interdisciplinary areas

Phonon resonance modulation in weak van der Waals heterostructures: Controlling thermal transport in graphene–silicon nanoparticle systems

Yi Li(李毅)[†], Yinong Liu(刘一浓)[†], and Shiqian Hu(胡世谦)[‡]

School of Physics and Astronomy, Yunnan University, Kunming 650091, *China*

(Received 19 November 2023; revised manuscript received 3 December 2023; accepted manuscript online 13 December 2023)

The drive for efficient thermal management has intensified with the miniaturization of electronic devices. This study explores the modulation of phonon transport within graphene by introducing silicon nanoparticles influenced by van der Waals forces. Our approach involves the application of non-equilibrium molecular dynamics to assess thermal conductivity while varying the interaction strength, leading to a noteworthy reduction in thermal conductivity. Furthermore, we observe a distinct attenuation in length-dependent behavior within the graphene–nanoparticles system. Our exploration combines wave packet simulations with phonon transmission calculations, aligning with a comprehensive analysis of the phonon transport regime to unveil the underlying physical mechanisms at play. Lastly, we conduct transient molecular dynamics simulations to investigate interfacial thermal conductance between the nanoparticles and the graphene, revealing an enhanced thermal boundary conductance. This research not only contributes to our understanding of phonon transport but also opens a new degree of freedom for utilizing van der Waals nanoparticle-induced resonance, offering promising avenues for the modulation of thermal properties in advanced materials and enhancing their performance in various technological applications.

Keywords: thermal conductivity, molecular dynamics, phonon resonance, van der Waals interaction, graphene–silicon nanoparticle heterostructure

PACS: 74.25.fc, 43.20.Ks, 65.80.Ck **DOI:** 10.1088/1674-1056/ad1501

1. Introduction

The miniaturization of electronic devices has escalated the urgency of addressing thermal management issues in these systems. Consequently, the optimization of heat transport, particularly in practical applications, has become the linchpin of effective thermal management, enhancing energy efficiency and advancing the development of next-generation materials.[1–5] Within the burgeoning field of heat transport studies, researchers have predominantly focused on exploring the dual facets of particle dynamics[6–8] and wave mechanics[9–11] pertaining to phonons. Remarkable progress has been achieved in controlling mid-frequency and high-frequency phonons through these methodologies.[12–15] However, the formidable challenge of taming low-frequency phonons persists, despite their significant contribution to the overall heat transport process.

The investigation of resonance modulation has emerged as a promising avenue in our pursuit of harnessing control over the low-frequency phonons.[16–18] Conventionally, this involves the introduction of pillar branches into the substructure, facilitating the interference of incident and reflected waves within the resonance structure.[19–23] This interference, coupled with the phonon band anti-crossing effect and hybridization with phonons in the substructure, gives rise to the formation of the flat bands. This, in turn, leads to a substantial reduction in the group velocity and relaxation time of phonons, consequently diminishing the overall thermal conductivity of the system.[24] Furthermore, the resonance offers a dynamic method to manipulate phonon transport by finely adjusting specific structural parameters, rendering it a central focus of recent research endeavors.

Nevertheless, while considerable strides have been achieved in this domain, it is crucial to highlight that the predominant focus of research on resonance-modulated phonon transport has centered on modifying resonant bonds within material structures.[17,22,24] Notably, these resonant structures are covalently linked to substructures, severely constraining the degree of freedom for modulation. Furthermore, the burgeoning field of van der Waals (vdW) integrated heterostructures has garnered significant attention, finding diverse applications in emerging fields such as optoelectronics,[25] nanoelectronics,[26] and quantum information.[27] Notably, researchers have recently uncovered highly anisotropic vdW thermal conductors within these heterostructures.[28] These compelling advancements have heightened our interest, prompting an exploration of the intriguing question of whether weak van der Waals forces themselves can instigate resonance

[†]These authors contributed equally to this work.

[‡]Corresponding author. E-mail: shiqian@ynu.edu.cn

© 2024 Chinese Physical Society and IOP Publishing Ltd

and, consequently, serve as a novel avenue for modulating phonon transport in previously uncharted ways.

In this study, we delve into the realm of phonon transport modulation within graphene by introducing silicon nanoparticles influenced by van der Waals forces. Our approach involves the application of non-equilibrium molecular dynamics (NEMD) to assess thermal conductivity while varying the interaction strength, leading to a noteworthy reduction in thermal conductivity. Furthermore, we observe a distinct attenuation in length-dependent behavior within the graphene–nanoparticles system. Our exploration combines wave packet simulations with phonon transmission calculations, aligning with a comprehensive analysis of the phonon transport regime to unveil the underlying physical mechanisms at play. Lastly, we conduct transient molecular dynamics simulations to investigate thermal boundary conductance (TBC) between the nanoparticles and the graphene, revealing an enhanced TBC. This study not only enhances our comprehension of phonon transport but also introduces a novel avenue for leveraging van der Waals nanoparticle-induced resonance. This discovery presents promising opportunities for manipulating thermal properties in advanced materials, thereby improving their performance across a range of technological applications.

2. Modeling and methodology

The supercell of the graphene-silicon nanoparticles heterostructure consists of a single-layer graphene (SLG) and silicon particles, as shown in Fig. 1(a), where carbon atoms are denoted by red and green, and silicon atoms are represented in blue. The length of the cell is 60 Å and 38 Å in the x and y directions. To maintain a suitable separation between the silicon nanoparticles and the graphene layer, we initially set the gap at 3.6 Å, while a 100 Å vacuum layer in the z-direction serves to prevent interactions between adjacent layers. In our model, we employ the optimized Tersoff potential[29] to capture the interactions among carbon atoms within graphene, while silicon–silicon interactions within the silicon nanoparticles are described using their original potential.[30] Furthermore, the interatomic interactions between carbon and silicon atoms are characterized using the Lennard–Jones (LJ) potential. The LJ potential expression is as follows:

$$V_{(r_{ij})} = \chi 4\varepsilon \left[\left(\frac{\sigma_{ij}}{r_{ij}} \right)^{12} - \left(\frac{\sigma_{ij}}{r_{ij}} \right)^{6} \right], \tag{1}$$

where r_{ij} represents the distance between atom i and atom j, ε denotes the energy constant, and σ_{ij} is the distance constant.[31] We set ε to 0.01782 eV and σ to 3.6286 Å, representing the interaction parameters between silicon and carbon atoms.[32–34] To investigate the influence of interlayer vdW interactions on the in-plane thermal conductivity of the graphene–silicon nanoparticle heterostructure, we introduce a variable factor denoted as χ. The χ value spans a range from 1 to 5. It's worth noting that there are no bonding interactions among separate silicon nanoparticles due to their substantial distance beyond the LJ cutoff distance. In our simulation, we only adjust the χ value within the green atomic region of graphene to emulate changes in vdW interactions, while the potential field of the red atomic region remains constant. This choice ensures that the silicon nanoparticles remain in stable positions throughout the simulation and precludes any potential interactions among them.

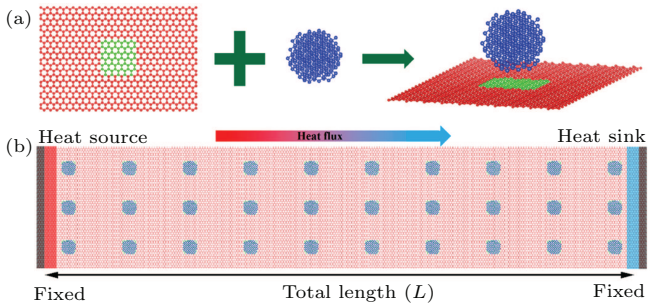


Fig. 1. Schematic representation of the supercell for the graphene–silicon nanoparticles heterostructure and its simulation model. (a) Top views of the unit cell of the Si–graphene heterostructure. (b) The NEMD simulation model used for thermal conductivity calculations.

In all NEMD calculations for this study, we employ the LAMMPS packages.[35] The NEMD simulation model is illustrated in Fig. 1(b), featuring a fixed system size of 60 nm×11.5 nm and comprising 30-unit cells. We set the length at 60 nm in our simulations, as the thermal transport in our system deviates from diffusive behavior. Consequently, the results reflect the effective thermal conductivity specific to this length. This methodology, widely utilized in literature, provides a robust means of determining effective thermal conductivity in finite-size systems.[36–38] The periodic and free boundary conditions are applied in the y and z directions, respectively, while a fixed boundary condition is maintained in the x direction. We employ the isothermal-isobaric (NPT) ensembles[39] for a duration of 50 ps to achieve structural relaxation and thermal equilibrium. To establish a consistent temperature gradient, two Langevin thermostats are connected to the two ends of the simulation system, operating at different temperatures, T_{H} and T_{L}. Specifically, T_{H} is set to 320 K, T_{L} to 280 K, with the thermal conductivity being calculated at 300 K. Once the system reaches a steady state, the cumulative energy (ΔE) added or subtracted in the heat source/sink region is recorded over a 5 ns interval, with a time step of 0.5 fs. The energy change per unit of time is determined through linear fitting of the accumulated energy (ΔE), subsequently employed to calculate the heat flux (J) using the formula $J = \Delta E/(\Delta t \cdot S)$. The thermal conductivity (κ) is calculated in accordance with Fourier's law, expressed as $\kappa = -J/\nabla T$, where S represents

the cross-sectional area and ∇T signifies the temperature gradient along the x direction.

3. Results and discussion

As illustrated in Fig. 2(a), the thermal conductivity of the graphene–silicon heterostructure exhibits a notable decline as the χ value increases. Notably, when χ equals 5, the thermal conductivity decreases to only 40% of that observed in the SLG. Intriguingly, despite the fact that vdW interactions are orders of magnitude weaker than covalent bonds,[40] the interaction strength remains significantly lower even as we increase the χ value to 5. When compared to the resonance modulation achieved through covalent bonds, it becomes evident that even weak vdW interactions can efficiently and conveniently alter the thermal conductivity by adjusting the χ value. This pivotal discovery constitutes a key finding of our study.

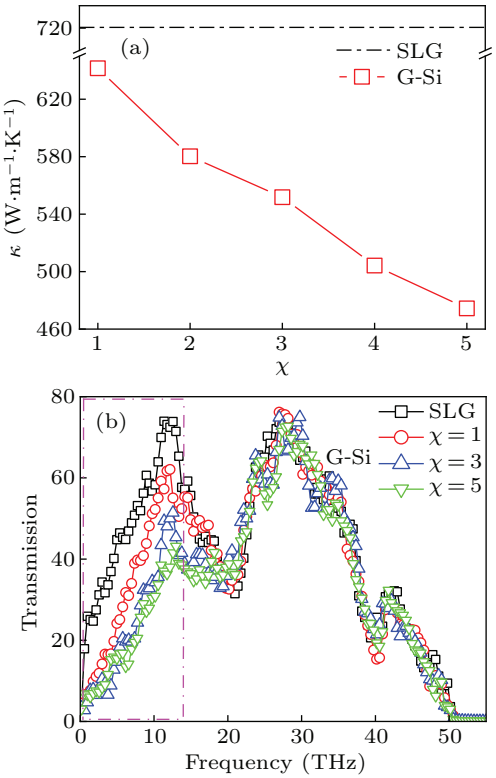


Fig. 2. The thermal conductivity results for the graphene–silicon nanoparticles heterostructure and its corresponding phonon transmission. (a) The thermal conductivity of the SLG and graphene–silicon nanoparticles heterostructure at different χ values. (b) The phonon transmission of SLG and Si–graphene heterostructure at different χ values; the pink dotted box indicates the low-frequency range where the phonon transmission exhibits a significant difference.

To investigate the reduction in thermal conductivity, we conduct an analysis of phonon transmission. The employed molecular dynamics calculations allow us to consider all orders of anharmonic interactions. The phonon transmission, denoted as $\Gamma(\omega)$, is calculated using the formula[41]

$$\Gamma(\omega) = \frac{q(\omega)}{k_{\mathrm{B}}\Delta T}, \tag{2}$$

where k_{B} represents the Boltzmann constant and ΔT indicates the temperature variance between the two Langevin thermostats. The calculation of $q(\omega)$, representing the heat flow across the cross-section, involves the formula[42]

$$q(\omega) = \frac{2}{M\Delta t}\,\mathrm{Re}\sum_{i\in L}\sum_{j\in R}\left\langle \hat{F}_{ij}(\omega)\hat{v}_i(\omega)^*\right\rangle, \tag{3}$$

with Δt denoting the time interval between samples obtained during the simulation and M representing the number of samples. The components $\hat{F}_{ij}(\omega)$ and $\hat{v}_i(\omega)^*$ represent the Fourier transformations of the total interactions and the velocity of the atom, respectively. Within the simulated structure, L and R denote the left and right ends of the virtual interface.

Figure 2(b) illustrates the pronounced suppression of phonons with frequencies below 13 THz, with minimal influence on mid- and high-frequency phonons. This remarkable reduction in low-frequency phonon transport is an exclusive outcome of the suppressive behavior of the phonon resonance structure. Achieving this outcome through conventional phonon scattering mechanisms has proven challenging due to the long-wavelength nature of low-frequency phonons, which typically exhibit behavior resembling ballistic transport. Notably, low-frequency phonons significantly contribute to graphene's thermal conductivity compared with their high-frequency counterparts. As the χ values increase, the phonon transmission coefficient within the low-frequency range decreases, offering a compelling explanation for the rapid decline in thermal conductivity with enhanced vdW interaction strength. Furthermore, given the crucial role played by out-of-plane phonons in the overall thermal conductivity of graphene,[43] we conjecture an increased likelihood of a more pronounced suppression of out-of-plane phonons contributing to the significant reduction in thermal conductivity.

However, the underlying physical mechanism behind this reduction in the low-frequency phonon transmission has remained elusive. To gain deeper insights into this phenomenon, particularly whether the decline in low-frequency phonon transport follows a diffusive or localized pattern, we conduct a phonon wave packet simulation within the graphene–silicon nanoparticle heterostructure.[44–46] We consider two scenarios with interaction strengths $\chi = 1$ and $\chi = 5$ for comparison. A similar wave packet simulation is performed within an SLG to provide a basis for comparison. Prior to launching the wave packet, we relax each structure using the NPT ensemble at 0 K to eliminate non-harmonic phonon–phonon scattering effects.[45,47] Periodic boundary conditions are applied in all directions, with an additional vacuum layer in the perpendicular direction.

The initial wave packet is constructed through linear combinations of normal vibration modes, formulated as[48,49]

$$\mu_{n,\alpha} = \mathrm{Re}\left\{A\varepsilon_{j\alpha,\lambda}\,\mathrm{e}^{\mathrm{i}k_0(x_n-x_0)}\,\mathrm{e}^{-(x_n-x_0)^2/\eta^2}\right\}. \tag{4}$$

To initialize velocities, we introduce time dependence and differentiate it as

$$v_{n,\alpha} = \mathrm{Re}\{-\mathrm{i}\omega_\lambda \mu_{n,\alpha}\}. \tag{5}$$

Here, $\mu_{n,\alpha}$ represents the αth displacement component of the atom in the simulated structure. A stands for the amplitude of the wave packet, η signifies the spatial width of the wave packet, and $\varepsilon_{j\alpha,\lambda}$ corresponds to the αth eigenvector component of the eigenmode λ for the jth atom in the graphene. x_n denotes the coordinate of the nth atom within the structure, and x_0 determines the center of the wave packet.

In our wave packet simulation, we specifically choose a transverse acoustic (TA) phonon with a frequency of 3.08 THz. To ensure ample space for wave packet transmission, we extend the length of the graphene to 1000 nm, with the silicon nanoparticles positioned in the region between 400 nm and 600 nm. The initial wave packet is generated at approximately 290 nm, which we refer to as the "initial moment," as depicted in Fig. 3(a). As anticipated, within the SLG, the wave packet remains unaltered. Throughout its propagation, the amplitude of the initial wave packet remains constant. This phenomenon can be attributed to the negligible impact of non-harmonic phonon scattering in SLG at 0 K, facilitating ballistic phonon transport.[12] However, as the wave packet enters the domain containing the silicon nanoparticles, as depicted in Fig. 3(b), it undergoes significant transformations. The wave packet effectively divides into two parts, with one segment standing within the nanoparticle region and the other part continuing its trajectory into the region on the right away from the nanoparticles. This phenomenon of confinement serves as a robust indicator of phonon resonance and its associated localization. Furthermore, when we increase the interaction strength χ to a value of 5, a larger portion of the wave packet becomes ensnared within the nanoparticle region, consequently leaving a reduced segment that could progress within the graphene region in Fig. 3(c). These observations closely align with the outcomes derived from our thermal conductivity calculations, offering tangible evidence of phonon resonance taking place within heterostructures featuring weak vdW interactions.

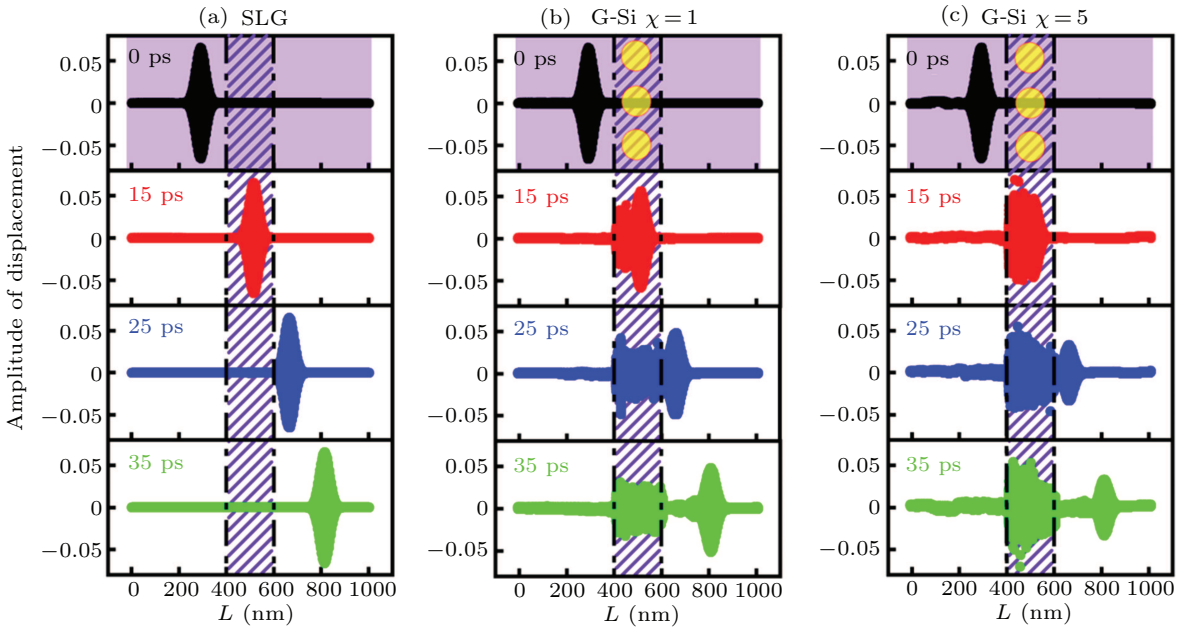


Fig. 3. Phonon wave-packet simulations in various structures. The simulations are conducted at 0 K. Snapshots of displacement for a TA wave packet in (a) SLG, (b) graphene–silicon nanoparticles with $\chi = 1$, and (c) graphene–silicon nanoparticles with $\chi = 5$. The shaded region from 400 nm to 600 nm indicates where the silicon nanoparticles are positioned in (b) and (c).

As the wave packet simulation can only depict the transport of a single phonon mode at one time, we delve deeper into understanding the transport state of low-frequency phonons under vdW resonance by calculating phonon transmission of the graphene–silicon nanoparticles heterostructure with varying lengths. The findings reveal a pronounced decrease in the transmission as the system length increases in Fig. 4(a). Previous studies have shown that such phonons adopt localized transport states when the transmission coefficient decreases exponentially with length.[50–52] To further elucidate this relationship, we fit the dependence between the phonon transmission coefficient and length at each frequency using the formula $\Gamma(\omega) = A\mathrm{e}^{-L/\xi}$. Here, L is the system length, and ξ is the localization length.[53] This formalism has been consistently applied in numerous previous studies for identifying Anderson localization.[54,55] We selectively consider results with a coefficient of determination, R^2, greater than 0.95.[56] The fitting results demonstrate that phonons in the 7–13 THz range in the graphene–silicon nanoparticles heterostructure are notably localized compared to single-layer graphene in Fig. 4(a). Additionally, as depicted in Fig. 4(b), the localized low-frequency phonons contribute to a further

suppression of the length-dependent thermal conductivity in the graphene–silicon nanoparticles heterostructure, which converges noticeably when the system length reaches 400 nm. This stands in stark contrast to the non-Fourier property of thermal conductivity in the SLG, where the thermal conductivity is $\log(L)$-dependent on the length L. The pronounced length dependence observed is primarily attributed to the contribution of low-frequency phonons. In single-layer graphene, low-frequency phonons exhibit an extended mean free path, resulting in the noticeable length dependence observed. Conversely, within the graphene–silicon nanoparticle system, the contribution of low-frequency phonons to thermal transport is mitigated by localization, thereby accounting for the suppressed length dependence of thermal conductivity in this particular system.[48] Furthermore, recent studies[57,58] propose that determining phonon Anderson localization can involve observing variations in thermal conductivity with thickness, specifically noting whether it exhibits an initial increase followed by an exponential decrease. It is essential to highlight that these observations were made by examining the interplay between the thermal conductivity contributions of coherent phonons and thickness variations after introducing randomness in the phononic crystal. This distinction between coherent and incoherent phonons was crucial in previous investigation.[48] However, our current study does not differentiate between these phonon types, and thus, similar phenomena have not been observed. Nonetheless, this aspect presents a promising avenue for future research.

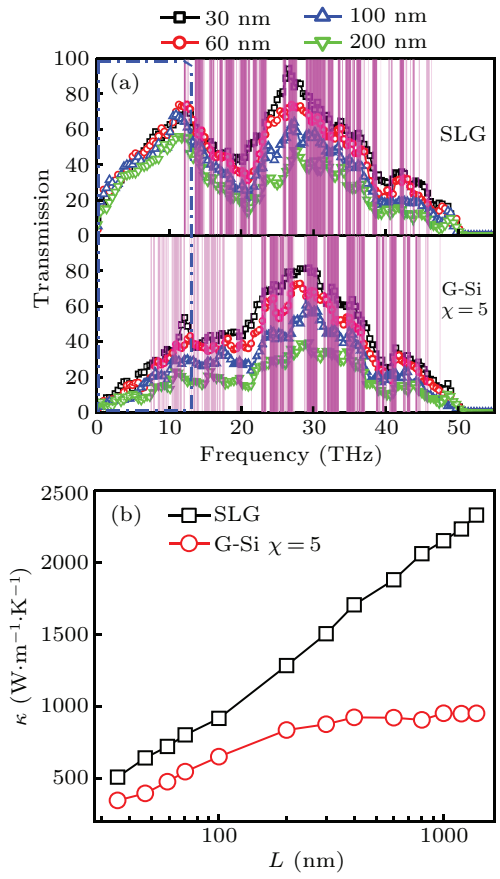


Fig. 4. The phonon transmission, corresponding localized phonon region, and length dependence of the thermal conductivity. (a) The phonon transmission results for the SLG and the graphene–silicon nanoparticles heterostructure with $\chi = 5$ with varying length. The pink vertical lines represent the phonon localized regime, and the blue dotted box denotes the low-frequency range where SLG lacks localized modes. (b) The length dependence of thermal conductivity for SLG and the graphene–silicon nanoparticles heterostructure with $\chi = 5$.

Moreover, considering the noticeable reduction in the in-plane thermal conductivity of graphene as χ increases, an important question emerges concerning its out-of-plane thermal properties. This inquiry gains significance given the pronounced phonon resonance effects induced by heightened χ, substantially influencing van der Waals interactions. To address this, we conduct calculations for the interfacial thermal conductance (ITC) between silicon and graphene using transient non-equilibrium molecular dynamics (TNEMD) methods.[59–61] This approach bears resemblance to experimental techniques involving laser pulses for nanoparticle heating.

The TNEMD simulations use LAMMPS, and a timestep of 0.5 fs is utilized within the NVE ensemble. As shown in Fig. 5(a), the temperatures of graphene and silicon are initially held at 300 K and 500 K, respectively, using a Langevin thermostat for 500 ps. Subsequently, the Langevin thermostat is deactivated, and temperature changes in graphene and silicon are recorded over an additional 500 ps period. Due to significant statistical temperature fluctuations, we average the results across 10 separate trajectories to ensure reliability and precision. Moreover, as illustrated in Fig. 5(b), the temperature profiles depicting the difference between silicon and graphene after the removal of the Langevin thermostat are examined. These profiles are fitted with an exponential function to accurately determine the time decay constant (τ). Notably, a larger or smaller value of τ signifies a longer or shorter time required for the system to reach thermal equilibrium, indicating a lower or higher ITC. The specific formula utilized for this purpose is as follows:

$$\Delta T = \Delta T\,(t_0)\,\mathrm{e}^{(t_0-t)/\tau}. \tag{6}$$

Subsequently, the ITC value is calculated using the following equation:

$$G = \frac{C_{\mathrm{H}}}{A \times \tau}. \tag{7}$$

Here, A represents the contact area between the silicon and graphene layers, approximately half of the silicon nanoparticle's surface area that defines the thermal interaction zone at the interface. Concurrently, C_{H} is defined as the effective constant volume heat capacity of the heterostructure, considering the combined thermal properties of the interfacing materials, and quantitatively described as follows:

$$C_{\mathrm{H}} = \frac{C_{\mathrm{Si}} C_{\mathrm{Gra}}}{C_{\mathrm{Si}} + C_{\mathrm{Gra}}}, \tag{8}$$

where C_{Si} and C_{Gra} represent the heat capacities of silicon and graphene, respectively.

The ITC within the graphene–silicon nanoparticle heterostructure is illustrated in Fig. 5(c), with χ as the variable. Notably, the ITC within the graphene–silicon nanoparticle heterostructure increases as χ increases. This phenomenon can be explained by two key mechanisms. First, the amplification of χ leads to the reinforcement of vdW interactions between the graphene and silicon nanoparticle layers. This, in turn, directly augments the phonon couplings between the graphene and silicon nanoparticles, thereby facilitating an improvement in the interfacial thermal transport. Secondly, the silicon nanoparticles effectively serve as resonance centers for in-plane phonons transport within the graphene layer. This results in the conversion of thermal energies carried by in-plane phonons into flexural phonon (out-of-plane) modes, ultimately strengthening the coupling between out-of-plane phonons and the silicon nanoparticles within the graphene layer.[62] As a result, this enhances the dissipation of thermal energy from silicon nanoparticle layer to the graphene layer in the graphene–silicon nanoparticle heterostructure.

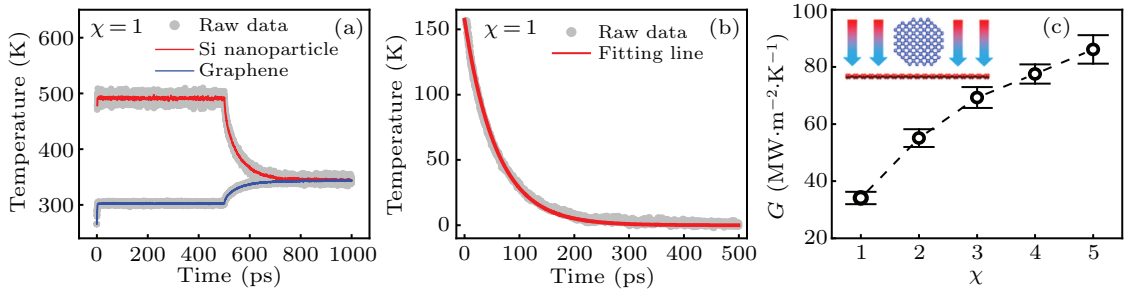


Fig. 5. The temperature evolution, fitting process, and the ITC results. (a) Temperature evolution profiles of graphene and silicon nanoparticles. (b) Temperature profiles showing the difference between silicon and graphene following the removal of the Langevin thermostat control. (c) The ITC results between graphene and silicon nanoparticles with varying χ.

4. Summary

In our study, we explored the phenomenon of phonon resonance in weak vdW interactions within graphene–silicon nanoparticle heterostructures. By enhancing the vdW interactions between silicon nanoparticles and graphene, we achieved a significant 40% reduction in thermal conductivity. Our findings, supported by phonon transmission calculations and wave packet simulations, offer compelling evidence of phonon resonance's potency in suppressing low-frequency phonons and lowering thermal conductivity. Additionally, our research revealed that the introduction of silicon nanoparticles led to a faster convergence of graphene's thermal conductivity with system length, due to an increase in low-frequency phonon localization modes. Furthermore, we investigated the interfacial thermal conductance between graphene and silicon nanoparticles, demonstrating that heightened vdW interaction strength improves the interfacial phonon transport by enhancing the coupling between in-plane and flexural phonon modes. Overall, this study advances our understanding of how weak van der Waals interactions can effectively control thermal transport through phonon resonance. These findings open new possibilities for the design of thermal materials and devices, offering innovative applications in the field.

Acknowledgements

This research was funded in parts by the National Natural Science Foundation of China (Grant No. 12105242) and Yunnan Fundamental Research Project (Grant Nos. 202201AT070161 and 202301AW070006). Y. Li, Y. Liu and S. Hu acknowledge support from the Graduate Scientific Research and Innovation Fund of Yunnan University (Grant No. KC-22221060).

References

[1] Jiang J, Zhang L, Ming C, *et al*. 2022 *Nature* **607** 480
[2] LaPotin A, Schulte K L, Steiner M A, Buznitsky K, Kelsall C C, Friedman D J, Tervo E J, France R M, Young M R, Rohskopf A, Verma S, Wang E N and Henry A 2022 *Nature* **604** 287
[3] Liu W, Liu Y, Yang Z, *et al*. 2023 *Nature* **617** 717
[4] Du T, Xiong Z, Delgado L, Liao W, Peoples J, Kantharaj R, Chowdhury P R, Marconnet A and Ruan X 2021 *Nat. Commun.* **12** 4915
[5] Qian X, Zhou J and Chen G 2021 *Nat. Mater.* **20** 1188
[6] Han S, Dai S, Ma J, Ren Q, Hu C, Gao Z, Duc Le M, Sheptyakov D, Miao P, Torii S, Kamiyama T, Felser C, Yang J, Fu C and Zhu T 2023 *Nat. Phys.* **19** 1649
[7] Britt T L and Siwick B J 2023 *Phys. Rev. B* **107** 214306
[8] Han Z and Ruan X 2023 *Phys. Rev. B* **108** 121412
[9] Ma D, Arora A, Deng S, Xie G, Shiomi J and Yang N 2019 *Mater. Today Phys.* **8** 56
[10] Feng L, Shiga T, Han H, Ju S, Kosevich Y A and Shiomi J 2017 *Phys. Rev. B* **96** 220301
[11] Giri A and Hopkins P E 2018 *Phys. Rev. B* **98** 045421
[12] Ding X and Ming Y 2014 *Chin. Phys. Lett.* **31** 046601
[13] Chen Z, Ge B, Li W, Lin S, Shen J, Chang Y, Hanus R, Snyder G J and Pei Y 2017 *Nat. Commun.* **8** 13828
[14] Asfandiyar, Cai B, Zhuang H L, Tang H and Li J F 2020 *Nano Energy* **69** 104393
[15] Liu Y, Yue J, Liu Y, Nian L L and Hu S 2023 *Chin. Phys. Lett.* **40** 086301
[16] Davis B L and Hussein M I 2014 *Phys. Rev. Lett.* **112** 055505
[17] Honarvar H and Hussein M I 2016 *Phys. Rev. B* **93** 081412
[18] Ma D, Wan X and Yang N 2018 *Phys. Rev. B* **98** 245420
[19] Zhang H, Sun B, Hu S, Wang H, Cheng Y, Xiong S, Volz S and Ni Y 2020 *Phys. Rev. B* **101** 205418
[20] Wang H, Cheng Y, Fan Z, Guo Y, Zhang Z, Bescond M, Nomura M, Ala-Nissila T, Volz S and Xiong S 2021 *Nanoscale* **13** 10010

[21] Li K, Cheng Y, Wang H, Guo Y, Zhang Z, Bescond M, Nomura M, Volz S, Zhang X and Xiong S 2022 *Int. J. Heat Mass Transf.* **183** 122144
[22] Honarvar H and Hussein M I 2018 *Phys. Rev. B* **97** 195413
[23] Liu H, Li W, Cao Z, Huang X and Ni Y 2023 *Int. J. Heat Mass Transf.* **205** 123903
[24] Xiong S, Sääskilahti K, Kosevich Y A, Han H, Donadio D and Volz S 2016 *Phys. Rev. Lett.* **117** 025503
[25] Zhang S, Liu Y, Sun Z, Chen X, Li B, Moore S L, Liu S, Wang Z, Rossi S E, Jing R, Fonseca J, Yang B, Shao Y, Huang C, Handa T, Xiong L, Fu M, Pan T, Halbertal D, Xu X, *et al*. 2023 *Nat. Commun.* **14** 6200
[26] Song Q, Occhialini C A, Ergeçen E, Ilyas B, Amoroso D, Barone P, Kapeghian J, Watanabe K, Taniguchi T, Botana A S, Picozzi S, Gedik N and Comin R 2022 *Nature* **602** 601
[27] Lee W, Fernandez-Mulligan S, Tan H, Yan C, Guan Y, Lee S H, Mei R, Liu C, Yan B, Mao Z and Yang S 2023 *Nat. Phys.* **19** 950
[28] Kim S E, Mujid F, Rai A, Eriksson F, Suh J, Poddar P, Ray A, Park C, Fransson E, Zhong Y, Muller D A, Erhart P, Cahill D G and Park J 2021 *Nature* **597** 660
[29] Lindsay L and Broido D A 2010 *Phys. Rev. B* **81** 205441
[30] Tersoff J 1988 *Phys. Rev. B* **37** 6991
[31] Johnson J K, Zollweg J A and Gubbins K E 2006 *Mol. Phys.* **78** 591
[32] Rappe A K, Casewit C J, Colwell K S, Goddard III W A and Skiff W M 1992 *J. Am. Chem. Soc.* **114** 10024
[33] Liang T, Zhang P, Yuan P and Zhai S 2018 *Phys. Chem. Chem. Phys.* **20** 21151
[34] Liang T, Zhou M, Zhang P, Yuan P and Yang D 2020 *Int. J. Heat Mass Transf.* **151** 119395
[35] Plimpton S 1995 *J. Comput. Phys.* **117** 1
[36] Chang C W, Okawa D, Garcia H, Majumdar A and Zettl A 2008 *Phys. Rev. Lett.* **101** 075903
[37] Yang N, Zhang G and Li B 2010 *Nano Today* **5** 85
[38] Lee V, Wu C H, Lou Z X, Lee W L and Chang C W 2017 *Phys. Rev. Lett.* **118** 135901
[39] Hoover W G 1985 *Phys. Rev. A* **31** 1695
[40] Liu Y, Weiss N O, Duan X D, Cheng H C, Huang Y and Duan X F 2016 *Nat. Rev. Mater.* **1** 16042
[41] Sääskilahti K, Oksanen J, Volz S and Tulkki J 2015 *Phys. Rev. B* **91** 115426
[42] Sääskilahti K, Oksanen J, Tulkki J and Volz S 2016 *Phys. Rev. E* **93** 052141
[43] Lindsay L, Broido D A and Mingo N 2010 *Phys. Rev. B* **82** 115427
[44] Hu M, Keblinski P and Schelling P K 2009 *Phys. Rev. B* **79** 104305
[45] Wei X and Luo T 2019 *J. Appl. Phys.* **126** 015301
[46] Wu M, Shi R, Qi R, Li Y, Feng T, Liu B, Yan J, Li X, Liu Z, Wang T, Wei T, Liu Z, Du J, Chen J and Gao P 2023 *Chin. Phys. Lett.* **40** 036801
[47] Lu Z, Smith N P, Prange M P, Bunker R A, Orrell J L and Chaka A M 2021 *Phys. Rev. Mater.* **5** 086002
[48] Hu S, Zhang Z, Jiang P, Chen J, Volz S, Nomura M and Li B 2018 *J. Phys. Chem. Lett.* **9** 3959
[49] Liu Y, Ren W, An M, Dong L, Gao L, Shai X, Wei T, Nie L, Hu S and Zeng C 2022 *Front. Mater.* **9** 913764
[50] Ni Y, Zhang H, Hu S, Wang H, Volz S and Xiong S 2019 *Int. J. Heat Mass Transf.* **144** 118608
[51] Roy Chowdhury P, Reynolds C, Garrett A, Feng T, Adiga S P and Ruan X 2020 *Nano Energy* **69** 104428
[52] Sun L, Zhai F, Cao Z, Huang X, Guo C, Wang H and Ni Y 2023 *Chin. Phys. B* **32** 056301
[53] Savić I, Mingo N and Stewart D A 2008 *Phys. Rev. Lett.* **101** 165502
[54] Mendoza J and Chen G 2016 *Nano Lett.* **16** 7616
[55] Juntunen T, Vänskä O and Tittonen I 2019 *Phys. Rev. Lett.* **122** 105901
[56] Nagelkerk E N J D 1991 *Biometrika* **78** 691
[57] Zhang Z, Guo Y, Bescond M, Chen J, Nomura M and Volz S 2021 *APL Mater.* **9** 081102
[58] Guo Y, Bescond M, Zhang Z, Xiong S, Hirakawa K, Nomura M and Volz S 2021 *APL Mater.* **9** 091104
[59] Ong Z Y and Pop E 2010 *Phys. Rev. B* **81** 155408
[60] Wu S, Wang J, Xie H and Guo Z 2020 *Energies* **13** 5851
[61] Rajabpour A, Seif R, Arabha S, Heyhat M M, Merabia S and Hassanali A 2019 *J. Chem. Phys.* **150** 114701
[62] Ma H, Babaei H and Tian Z 2019 *Carbon* **148** 196